PCCP

ROYAL SOCIETY OF CHEMISTRY

PAPER

View Article Online
View Journal | View Issue

Cite this: *Phys. Chem. Chem. Phys.*, 2025, **27**, 25053

Strategic functionalization of bromine and nitrogen at the bay region of perylene induces a heavy atom effect and promotes intersystem crossing

Pandiselvi Durairaj, Sonia Das and Sunandan Sarkar *

Received 14th August 2025,
Accepted 23rd October 2025

DOI: 10.1039/d5cp03115j

rsc.li/pccp

Spin–orbit coupling (SOC)-assisted intersystem crossing (ISC) plays a pivotal role in designing metal-free organic systems for optoelectronic applications. We computationally designed a new structural motif, *i.e.*, 12-bromo-1-azaperylene (12-BAP), which incorporates three crucial factors that promote rapid ISC: a change in state character during singlet–triplet conversion ($^1\pi\pi^* \rightarrow {}^3n\pi^*$), a pronounced heavy atom effect (HAE), and a favourable energy alignment between the $^1\pi\pi^*$ and $^3n\pi^*$ states. Notably, the close spatial positioning of the heavy Br atom near the site of orbital angular momentum change intensifies the HAE. As a result, a strong SOC (89 cm^{-1}) between the $^1\pi\pi^*$ and $^3n\pi^*$ states drives ultrafast ISC (10^{12} s^{-1}). In contrast, azaperylene and its 12-hydroxy derivatives exhibit limited ISC efficiency owing to the higher energetic position of the $^3n\pi^*$ state. Br substitution at the 12-position of 1-azaperylene yields the highest SOC and fastest ISC among all Br-substituted variants. Efficient triplet-state generation is crucial for the development of high-performance organic phosphorescent emitters and photodynamic therapeutic agents. The 12-BAP motif promotes ISC, providing a versatile scaffold for the rational design of functional organic materials.

Introduction

Harvesting triplet excitons in organic materials enable a wide range of optoelectronic applications, including organic light-emitting devices (OLEDs) and singlet oxygen ($^1O_2$) production for photodynamic therapy (PDT).[1–3] ISC is a unimolecular photophysical process that converts singlet to triplet excitons ($S_1 \rightarrow T_n$). Although ISC is a spin-forbidden transition, it becomes feasible through SOC, which leads to mixing of singlet and triplet states.[4] Hence, increasing SOC strength is crucial for achieving an efficient triplet population. For example, organometallic compounds of Pt(II), Ir(III), and Ru(II) metals often exhibit near-unity triplet quantum yields due to their large SOC generated by the heavy nucleus.[5,6] However, their large-scale production and vast application remain unattainable owing to their scarcity, high cost, and cytotoxicity. Researchers have focused on developing metal-free, purely organic materials capable of efficient triplet exciton generation through structural and crystal engineering to overcome these challenges.[7–14]

Heavier non-metal chalcogens and halogens enhance SOC and ISC in organic materials, reducing dependence on heavy metals.[15–21] Organic systems featuring aromatic carbonyls or nitrogen-containing heterocycles (bearing lone-pair electrons) facilitate ISC *via* pronounced SOC, which originates from a change in the nature of transition orbitals ($n\pi^* \leftrightarrow \pi\pi^*$) between initial and final excited states.[22,23] This process is known as the El-Sayed-allowed transition for the spin-flip process.[4,23] Since SOC implies that the spin (S) and orbital (L) angular momentum of an electron are coupled, a spin-flip transition must follow the orbital angular momentum change (ΔL) according to the law of angular momentum conservation.[20] A change in orbital character between the initial and final states can produce nonzero SOC, thereby allowing spin-forbidden singlet-to-triplet transitions. High SOC is associated with the $n\pi^* \leftrightarrow \pi\pi^*$ transition because the nonbonding (n) orbital lies perpendicular to the π-orbital, enabling electron spin flip *via* a 90° orbital rotation. In contrast, the $\pi\pi^* \rightarrow \pi\pi^*$ transition in a planar system exhibits negligible SOC and is known as an El-Sayed-forbidden process, since spin flip cannot occur without a change in orbital orientation. The increase in SOC within twisted π-conjugated frameworks is attributed to π-orbital mixing and the resultant effective orbital angular momentum.[24,25] Accordingly, non-planarity promotes state interactions that reinforce the $\pi\pi^* \rightarrow \pi\pi^*$ transition as an El-Sayed-allowed process.

Over the past decade, the Kim group has developed a strategy to enhance room-temperature phosphorescence (RTP)

Department of Chemistry, National Institute of Technology, Tiruchirappalli, Tamil Nadu, 620015, India. E-mail: ssarkar@nitt.edu

through non-covalent halogen bonding between the carbonyl moiety of 4-bromobenzaldehyde and the Br atom of a neighbouring molecule (C═O···Br).[7–9] A heavy Br nucleus near the nπ* site activates the intermolecular heavy atom effect (HAE), promoting ISC and RTP. Importantly, their crystal design principle imparts rigidity to the system, reducing energy loss *via* molecular vibrations. Sarkar *et al.* demonstrated an alternative approach wherein substitution of a heavy Br atom proximal to the C═O group orbitals enhanced ISC in *ortho*-bromobenzaldehyde.[26] This enhancement originates from intramolecular HAE, which operates effectively through lateral interactions between the orbitals of the Br atom and the C═O group. To date, various systems featuring heavy halogens near ΔL sites have been developed, wherein inter- or intramolecular HAEs play a pivotal role in boosting SOC and promoting the triplet-state population.[27–36] In this work, we focused on intramolecular HAE, facilitated by strategic substitution that places the heavy atom in close proximity to the key chromophoric orbitals.

Polyaromatic hydrocarbons, such as perylenes, are emerging as robust photosensitizers due to superior photostability and light absorption.[37] Rachford *et al.* reported fluorescence quenching *via* efficient ISC in Pt(II) complexes, where the Pt(II) center is coordinated in the bay region of two perylenediimide (PDI) units.[38] Heavy-metal-free strategies have been developed for triplet exciton formation to circumvent the need for expensive metals. For example, Tiley *et al.* revealed ultrafast triplet formation upon replacing oxygen atoms with heavier sulfur in PDI.[16] Lee *et al.* recently developed a thione-derived PDI–peptide bioconjugate that showed rapid ISC and served as a photosensitizer for bioimaging and PDT.[39] Wu *et al.* reported an ISC quantum yield exceeding 90% in fused di-PDI systems, which efficiently functioned as photosensitizers for $^1O_2$ generation.[40] Modifying the bay region of perylenes by Br atoms distorts the π-system, offering an effective approach to enhancing SOC and accelerating ISC.[41,42]

Interestingly, bay-region engineering of perylenes affords strategic control over optoelectronic properties. For example, nitrogen doping at these sites enhances molar absorptivity, fluorescence efficiency, and host–guest interactions.[43] Gryko *et al.* reported 1-azaperylene as a bright fluorophore with high optical emission,[44] while its hydroxy derivative (12-hydroxy-1-azaperylene) showed reduced fluorescence due to excited-state intramolecular proton transfer (ESIPT).[45] Hirono *et al.* synthesized mono- to tetra-azaperylenes *via* bay-position nitrogen substitution on perylene and observed a progressive decline in the fluorescence quantum yield with increasing nitrogen content due to enhanced nonradiative decay.[46]

In this work, we discussed the photophysical properties of a newly designed structural scaffold, in which halogens (F, Cl, and Br) are substituted at the 12-position of 1-azaperylene. The key objective is to elucidate how the heavy elements near the n-orbital of pyridinic-N promote the ISC and quench the fluorescence. Fig. 1 displays the pristine azaperylene (AP) and its 12-substituted derivatives (12-XAP). We estimated the fluorescence and ISC rate constants of these systems using

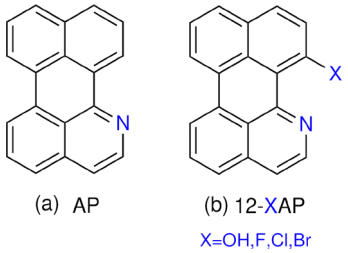

Fig. 1 1-Azaperylene (AP) and its 12-substituted derivatives (12-XAP).

theoretical and computational methods to predict the possible deactivation of the S_1 state. We further examined how the substitution of Br at different positions in AP modulates the electronic structure and provides a rationale for designing metal-free spin-conversion scaffolds *via* HAE.

Computational methods

Density functional theory (DFT) was used to optimize the ground state geometry for all systems.[47,48] Excited state properties were computed by employing time-dependent DFT (TDDFT) with Tamm–Dancoff approximation (TDA).[49–52] TDDFT often underestimates the energy of triplet states, which leads to inaccurate predictions of the energy gap between singlet and triplet states. The TDA approach overcomes this issue, offering more reliable results.[52] The range-separated hybrid (RSH) density functional ωB97X-D was employed in this study.[53,54] The ωB97X-D functional incorporates 22.2% short-range and 100% long-range exact Hartree–Fock (HF) exchange and offers balanced accuracy for predicting excitation energies for both local and nonlocal (*e.g.*, charge-transfer) excitons. We used the 6-31+G(d,p) basis set for geometry optimization and excitation energy calculations for all systems.[55] The state-tracking method was used to optimize the geometry of higher triplet excited states.[56] The SG-2 quadrature grid was employed for all calculations to ensure consistent numerical integration. A tight SCF convergence criterion (level 8) was used, corresponding to a wavefunction error below 10^{-8}, which guarantees reliable self-consistent field convergence. All molecules were treated with C_1 symmetry throughout all calculations. State characterization was performed based on orbital contributions and natural transition orbital (NTO) analysis, allowing the assignment of excited states according to their dominant electronic character (*e.g.*, π → π*, n → π*). The Q-Chem 5.4 package was used to perform all the calculations in the gas phase.[57]

The fluorescence quantum yield (Φ_{fl}) governs photoluminescence efficiency by quantifying the radiative and nonradiative decay rate constants, which is defined as

$$\Phi_{fl} = \frac{k_{fl}}{k_{fl} + \sum k_{nr}}, \quad (1)$$

where k_{fl} is the fluorescence rate constant and $\sum k_{nr}$ refers to the sum of nonradiative decay rate constants. Typically, k_{fl} is high when the S_1 state has high OS, while substantial SOC between S_1 and adjacent triplet states accelerates ISC,

increasing the triplet population. Thus, the estimation of ISC rate constants is crucial for a comprehensive understanding of the photophysical behaviour of AP and 12-XAP. The fluorescence rate constants (k_{fl}) were estimated using the Strickler–Berg equation:[12,58]

$$k_{fl} = 0.6671\ \left[\mathrm{cm^2\ s^{-1}}\right]\frac{\nu_{em}{}^3}{\nu_{ab}}f, \tag{2}$$

where f refers to the OS of the S_1 state and ν_{em} and ν_{ab} are the emission and absorption frequencies (in cm^{-1}), respectively. The ISC rate constants (k_{isc}) between S_1 and T_n states were calculated using the Marcus theory:[59]

$$k_{isc} = \frac{|V_{soc}|^2}{\hbar}\sqrt{\frac{\pi}{k_B T E_r}}\exp\left(-\frac{(E_r + \Delta G)^2}{4E_r k_B T}\right), \tag{3}$$

where E_r represents the reorganization energy, ΔG refers to the electronic energy difference between the T_n and S_1 states, and V_{soc} is the SOC matrix element computed at the S_1-geometry ($\langle S_1|\hat{H}_{so}|T_n\rangle$).[60] Here, T denotes the temperature used for ISC rate calculations, which is set at 300 K.

SOC introduces relativistic correction to the non-relativistic Hamiltonian, typically included through perturbative treatment. SOC enables state mixing and is thus essential for the description of key photophysical properties in molecular systems, for example, ISC. The Breit–Pauli Hamiltonian is utilized to compute the SOC matrix elements between non-relativistic electronic states. The form of the Breit–Pauli spin–orbit (SO) operator (in atomic units) is[61–64]

$$\mathbf{H}_{BP} = \sum_i \mathbf{h}_1 \cdot \mathbf{s}_i - \sum_{i\neq j}\mathbf{h}_2 \cdot (\mathbf{s}_i + 2\mathbf{s}_j), \tag{4}$$

where the first term represents the one-electron spin–orbit (SO) operator, in which $\mathbf{h}_1$ is expressed as

$$\mathbf{h}_1 \equiv \frac{\alpha_0{}^2}{2}\sum_A \frac{Z_A}{r_{Ai}{}^3}(\mathbf{r}_{Ai} \times \mathbf{p}_i),$$

and the second term represents the two-electron spin–own-orbit and spin–other-orbit (SOO) operator, in which $\mathbf{h}_2$ is expressed as

$$\mathbf{h}_2 \equiv \frac{\alpha_0{}^2}{2}\frac{1}{r_{ij}{}^3}(\mathbf{r}_{ij} \times \mathbf{p}_i).$$

Here, α_0 and Z_A denote the fine structure constant and nuclear charge of the Ath nucleus, respectively; r_{Ai} and r_{ij} are the distances between the ith electron and the Ath nucleus, and between electrons i and j, respectively; $\mathbf{p}$ and $\mathbf{s}$ are the momentum and spin operators.

The first term in eqn (4) captures one-electron SO effects, which grow strongly with Z and dominate in heavy atoms, while the two-electron term is appreciable in the case of light-atom systems, as it carries an opposite sign and a magnitude comparable to that of the one-electron term. However, a full evaluation of SOC is computationally expensive due to its two-electron term.[65] The computational burden can be mitigated by approximating the two-electron term with an effective one-electron SO operator of mean-field character.[62] Alternatively, two-electron effects are treated empirically in the one-electron SO operator by replacing the nuclear charge with effective value,[66] and accordingly eqn (4) is reduced to an effective one-electron SO operator of the form:

$$\mathbf{H}_{SO} \equiv \frac{\alpha_0^2}{2}\sum_A\sum_i \frac{Z_{eff}}{r_{Ai}^3}(\mathbf{r}_{Ai} \times \mathbf{p}_i) \cdot \mathbf{s}_i. \tag{5}$$

Here, Z_{eff} refers to the effective nuclear charge, empirically adjusted to match the experimentally determined fine-structure splittings (FSS) across different atoms.[66–68]

Koseki, Gordon, and co-workers notably determined Z_{eff} values for main group elements using the multiconfiguration self-consistent field method with relativistic effective core potentials (MCSCF/SBK).[66] They also formulated the scaling factor (Z_{eff}) using the MCSCF method with all-electron basis sets as follows:

$$Z_{eff} = y_m Z_A \tag{6}$$

$$y_1 = 0.45 + 0.05n \quad \text{for Li–F}$$

$$y_2 = 0.98 - 0.01n \quad \text{for Na–Cl}$$

$$y_3 = 1.21 - 0.03n \quad \text{for K, Ca, Ga–Br}$$

$$y_4 = 1.24 \quad \text{for Rb, Sr, In–I}$$

where n is the number of valence electrons. Thus, the Z_{eff} from all-electron calculations ranges from 0.5 to 1.24 times the true nuclear charge, depending on the element.

Chiodo and Russo derived the scaling factor *via* all-electron DFT calculations using the B3LYP functional and DZVP basis set.[69] Their formula defines the scaling factor as follows:

$$Z_{eff} = y_m Z_A \tag{7}$$

$$y_1 = 0.2516 + 0.0626n \quad \text{for B–F}$$

$$y_2 = 0.7213 + 0.0144n \quad \text{for Al–Cl}$$

$$y_3 = 0.8791 + 0.0039n \quad \text{for Ga–Br}$$

$$y_4 = 0.9228 + 0.0017n \quad \text{for In–I.}$$

Their study revealed that the FSS of diatomic systems calculated using Z_{eff} (B3LYP/DZVP) showed excellent agreement with full-operator results and experimental data. In this work, SOC matrix elements between singlet and triplet states were evaluated using the effective one-electron SO operator (eqn (5)) and Chiodo-derived Z_{eff} values (eqn (7)). The ωB97X-D functional and aug-cc-pVTZ all-electron basis set were used for these calculations.

Results and discussion

We calculated the absorption (E_{ab}) and emission (E_{em}) energies, specifically the vertical excitation energy of the S_1 state at both ground and S_1 state geometries, for AP and its derivatives

Table 1 Calculated absorption (E_{ab} in eV) and emission energies (E_{em} in eV) of the S_1 state, oscillator strength (f), and fluorescent rate constants (k_{fl} in s^{-1}) for AP and 12-XAP

Molecule	E_{ab}	f_{ab}	E_{em}	f_{em}	k_{fl}
AP	3.464	0.635	3.063	0.680	2.47×10^8
12-HAP	3.383	0.591	3.059	0.621	2.30×10^8
12-FAP	3.533	0.647	3.126	0.690	2.61×10^8
12-CAP	3.507	0.626	3.100	0.671	2.49×10^8
12-BAP	3.493	0.611	3.087	0.657	2.42×10^8

(12-XAP) (Fig. 1). In our earlier study, the E_{ab} and E_{em} of perylene were reported as 3.428 eV and 3.035 eV, respectively.[42] Replacing the bay C–H unit with pyridinic N has minimal impact on both the E_{ab} and E_{em} of AP, with values of 3.464 eV and 3.063 eV, respectively. Hirono *et al.* reported through their spectroscopic analysis that the optical spectra of perylene and AP exhibited remarkable similarity.[46] Nevertheless, substituents at the 12-position of AP can modulate electron distribution within the π-system, offering potential avenues for tuning its optoelectronic properties. Table 1 highlights the correlation between the electronic characteristics of the substituents and their influence on optical properties.

Hydroxy substitution at the 12-position of AP (12-HAP) resulted in a 0.08 eV redshift in E_{ab} compared to AP, while a slight redshift was observed in E_{em}. This trend aligns with previous experimental observations, though the experimentally measured values exhibited significantly larger redshifts.[44] The redshift is underestimated because the TDDFT calculations were performed without accounting for dielectric medium effects, whereas the experimental measurements were conducted in various solvents. Our computational data revealed that the redshift observed in 12-HAP originates from an increase in its HOMO energy level, attributed to the strong electron-donating effect of the OH group (Fig. S1). Furthermore, the OH group promoted more extensive π-conjugation in the HOMO of 12-HAP relative to AP. In the past, Deperasińska *et al.* reported a ~0.28 eV energy separation between E_{ab} and E_{em} in 12-HAP from gas-phase TDDFT-B3LYP calculations.[45] Our TDDFT calculations using the ωB97X-D functional in the gas phase estimated a 0.32 eV energy difference, closely matching the previous result.

In contrast, halogen substitution at the 12-position of AP (12-FAP, 12-CAP, and 12-BAP) exhibited blueshifts in both E_{ab} and E_{em} compared to AP. This effect arises from the electron-withdrawing nature of halogens, which influences FMOs and their energies (Fig. S1). The 0.07 eV blueshift in 12-FAP, the most pronounced among the halogenated derivatives, stems from the higher electronegativity of F. While larger halogens like Cl and Br typically reduce the energy gap relative to F, resulting in a less pronounced effect. The S_1 state of AP and 12-XAP originated from the HOMO → LUMO transition (Table S1), exhibiting a high transition dipole moment and substantial oscillator strength (OS). Consequently, their fluorescence rate constants ($k_{fl} \approx 10^8$ s^{-1}) are significant, as k_{fl} is directly proportional to OS according to the Strickler–Berg relationship.[12,58] The experimentally determined k_{fl} values for perylene and AP are 10^8 s^{-1}, indicating that the calculated k_{fl} value for AP aligns well with experimental results.[46] Prior experimental studies have demonstrated that AP and 12-HAP exhibit strong fluorescence.[45,46] To date, the synthesis and spectroscopic analysis of 12-halogenated AP derivatives have not been reported. This work used computational methods to predict the photophysical behaviour of 12-halogenated AP derivatives.

Our prior computational study on bromo-substituted perylenes, conducted using a comparable protocol, showed good agreement with experimental observations.[42] An experimental study reported high Φ_{fl} for perylene and its *ortho-* and *peri-*bromo derivatives (P-*o*Br and P-*p*Br), while *bay*-substitution (P-*b*Br) led to marked fluorescence quenching.[70] These trends were well rationalized through computational analysis, as summarized in Table 2. The calculated k_{fl} values for perylene and P-*p*Br are in good agreement with experimental measurements. To explain the high Φ_{fl} observed for perylene, P-*p*Br, and P-*o*Br, the computational study revealed that the corresponding k_{isc} values are negligible or 2–3 orders of magnitude lower than the k_{fl} value. Conversely, the low Φ_{fl} of P-*b*Br is theoretically linked to a two-order increase in ISC, promoted by high SOC resulting from *bay*-induced π-twisting. In the present work, our calculations are consistent with the experimentally measured k_{fl} and explained that the high Φ_{fl} of AP originated from its suppressed ISC.

To investigate the nonradiative decay *via* the ISC process, we first examined the potential ISC channels of AP and 12-XAP. SOC enables mixing between the unperturbed S_1 and T_n states, allowing the singlet state to acquire partial triplet character and *vice versa*. This admixture allows spin-forbidden ISC to occur with enhanced probability. The extent of this mixing, denoted by λ, is primarily determined by the energy difference between T_n and S_1 (ΔST) and the SOC strength. λ can be defined from the first-order perturbation theory as

$$\lambda = \frac{\langle S_1 | \hat{H}_{so} | T_n \rangle}{|\Delta ST|}.$$

Possible ISC channels for AP and 12-XAP were identified based on these two factors computed at the ωB97X-D/aug-cc-pVTZ level and are summarized in Table S2. The SOC matrix elements were computed using the effective one-electron SO operator (eqn (5)) with Chiodo-derived Z_{eff} values presented in Table S3.

Table 2 Experimentally measured Φ_{fl} and k_{fl} (exp.) (in s^{-1}) along with computed k_{fl} (theory) (in s^{-1}) and k_{isc} (theory) (in s^{-1})

Molecule	Φ_{fl}	k_{fl} (exp.)	k_{fl} (theory)	k_{isc} (theory)
Perylene	0.98[a]	1.78×10^8	2.37×10^8	
P-*p*Br	0.88[a]	2.02×10^8	2.57×10^8	5.53×10^6
P-*o*Br	0.89[a]		2.37×10^8	5.09×10^5
P-*b*Br	0.05[a]		1.89×10^8	4.28×10^{10}
AP	0.74[b]	1.1×10^8	2.47×10^8	1.96×10^7

[a] Lewitzka *et al.*[70] [b] Hirono *et al.*[46]

Table 3 Comparison of ΔST (in eV) and SOC (in cm^{-1}) between the $^1\pi\pi^*$ and $^3n\pi^*$ states of halogenated AP across all-electron basis sets. SOCs were computed using the effective one-electron SO operator with Chiodo-derived Z_{eff} values

	def2-TZVP		def2-TZVPD		aug-cc-pVTZ	
Molecule	ΔST	SOC	ΔST	SOC	ΔST	SOC
12-FAP	0.44	7.21	0.46	7.15	0.47	7.09
12-CAP	0.22	20.27	0.23	20.04	0.24	18.95
12-BAP	0.13	91.44	0.14	90.51	0.15	88.92

Table 3 presents the ΔST and SOC between the $^1\pi\pi^*$ and $^3n\pi^*$ states of halogenated AP, revealing basis set sensitivity on singlet–triplet gap and spin–orbit interactions. Inclusion of diffuse functions in the Karlsruhe triple-zeta basis set (def2-TZVPD)[71] slightly increased the ΔST without greatly affecting SOC for 12-FAP and 12-CAP. The Dunning correlation-consistent basis set (aug-cc-pVTZ)[72] exerted minimal impact on ΔST and showed a 1–1.5 cm^{-1} reduction in SOC for the heavier analogues (12-CAP and 12-BAP) relative to def2-TZVPD. The aug-cc-pVTZ includes extensive diffuse and high-angular-momentum polarization functions, offering more reliable SOC matrix elements for systems bearing heavier atoms.[73] Table S4 summarizes the ΔST and SOC between the $^1\pi\pi^*$ and $^3n\pi^*$ states of 12-BAP for different density functionals. The negative ΔST from PBE0 and B3LYP reflected their underestimation of the $^3n\pi^*$ state energy, whereas ωB97X-D and CAM-B3LYP provided more reliable energy alignment between $^1\pi\pi^*$ and $^3n\pi^*$ states, as range-separated hybrids better capture the excitation energies of charge-transfer or delocalized states such as $n\pi^*$. The SOC values obtained with PBE0 and B3LYP are about 20–30 cm^{-1} higher than those obtained using ωB97X-D and CAM-B3LYP. A prior theoretical study reported an SOC of 98 cm^{-1} between the $^1\pi\pi^*$ and $^3n\pi^*$ states in bromine-substituted naphthalenediimide (Br adjacent to the C=O group), calculated using the TDDFT/ωB97X-D/cc-pVTZ method and Chiodo-derived Z_{eff}.[74]

Fig. 2 shows that the T_1 state is positioned significantly below the S_1 state, leading to a large singlet–triplet energy gap (ΔST) across all systems. The $\langle S_1|\hat{H}_{so}|T_1\rangle$ is weak due to their identical state character ($\pi\pi^*$). Consequently, T_1 is not favourable for ISC due to low singlet–triplet mixing. The T_2 state is energetically proximal to S_1 for all systems, within the range of ±0.1 eV (Table S2), although SOC is low due to the $\pi\pi^*$ nature. Among the several low-lying triplet states, the T_6 of AP, T_8 of 12-HAP, T_4 of 12-FAP and 12-CAP, and T_3 of 12-BAP exhibited a different state character ($n\pi^*$) than the S_1 state (refer to Fig. 2). Thus, these triplet states produced significant SOC with the S_1 state, with a notable enhancement observed as the halogen size increases (7 cm^{-1} for 12-FAP, 19 cm^{-1} for 12-CAP, and 89 cm^{-1} for 12-BAP). However, these triplet states are positioned above the S_1 state, with a particularly large ΔST of 0.73 eV for AP and over 1.3 eV for 12-HAP at the S_1-geometry. In contrast, ΔST decreases with increasing halogen size, with values of 0.47 eV for 12-FAP, 0.24 eV for 12-CAP, and 0.15 eV for 12-BAP. This is because the energy of the non-bonding orbital (n) in 12-HAP is more stabilized than AP, while it increases with the size of the halogens (refer to Fig. S2).

Considering the ΔST and SOC values, the preferred triplet states for ISC are T_2 for AP and 12-HAP, T_4 for 12-FAP and 12-CAP, and T_3 for 12-BAP. Moreover, the proximity of T_2 in 12-FAP, 12-CAP, and 12-BAP supports its potential as a viable ISC state. T_6 in AP was considered for comparative evaluation due to its significant SOC. We calculated the ISC rate constants (k_{isc}) for these channels in AP and 12-XAP using the Marcus theory.[59,60,75] Details of k_{isc} for selected channels are provided in Table S5. The k_{isc} for the $S_1 \rightarrow T_2$ transition in AP is 1.96×10^7 s^{-1}, whereas for $S_1 \rightarrow T_6$, it is 8.06×10^6 s^{-1}. Despite a strong SOC (5.39 cm^{-1}) between S_1 and T_6, the ISC is slow due to an uphill transition ($\Delta G \approx 190$ meV) with a high energy barrier of ~244 meV. The k_{isc} for the $S_1 \rightarrow T_2$ transition in 12-HAP is 6.91×10^7 s^{-1}, three times higher than that of AP due to a lower energy barrier (2.5 meV) and higher SOC (0.46 cm^{-1}) compared to AP. For halogen-substituted AP, the k_{isc} for the $S_1 \rightarrow T_2$ transition is ~10^{7-8} s^{-1}. Although having a low energy barrier (<2 meV), the SOC of T_2 associated with S_1 is weak (~0.20 cm^{-1}). The k_{isc} for the $S_1 \rightarrow T_2$ transition of AP and 12-XAP is smaller than or comparable to their fluorescence rate

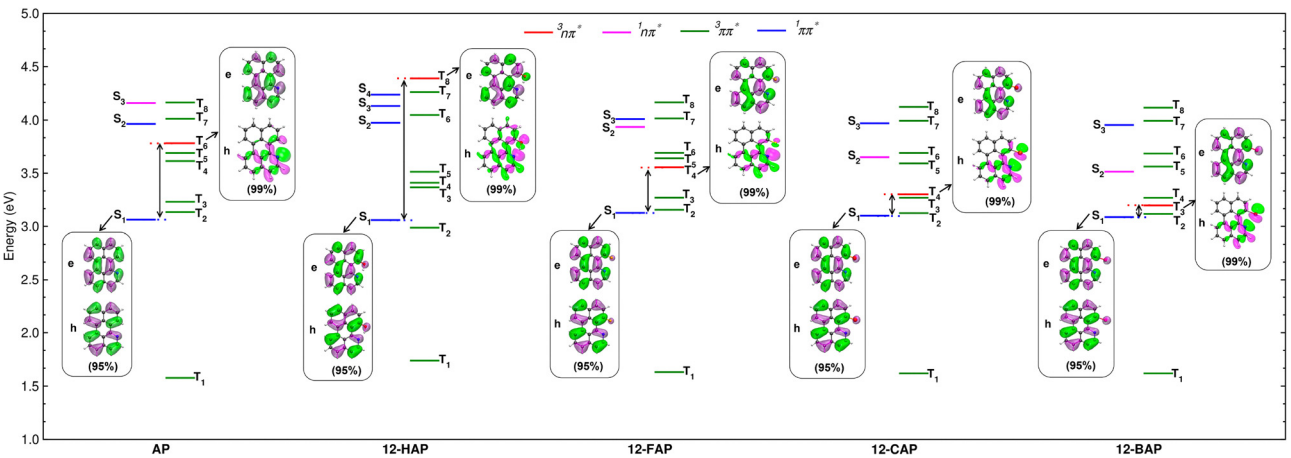

Fig. 2 Energy alignment of the singlet and triplet states of AP and 12-XAP at their S_1-geometry (ωB97X-D/6-31+G(d,p) level). Hole and electron natural transition orbitals (NTOs) for the S_1 ($^1\pi\pi^*$) and T_n ($^3n\pi^*$) states of AP and 12-XAP, with an isosurface value of 0.02.

constant ($k_{fl} \approx 10^8\ s^{-1}$). Hence, the $S_1 \rightarrow T_2$ ISC channel cannot outcompete the fluorescence of these systems.

Interestingly, the k_{isc} for the $S_1 \rightarrow T_4$ transition in 12-FAP and 12-CAP is $6.19 \times 10^8\ s^{-1}$ and $6.04 \times 10^{10}\ s^{-1}$, respectively. The $S_1 \rightarrow T_3$ transition in 12-BAP exhibited an ultrafast ISC rate, with a k_{isc} value of $2.22 \times 10^{12}\ s^{-1}$ (Table S5). This improvement of rates is attributed to the enhanced SOC driven by a change in state character following El-Sayed's rule and an energetically favourable process ($\Delta G < 0$). The effect is more pronounced in 12-BAP due to the heavy nucleus of Br near the region of orbital angular momentum change. In addition, the $S_1 \rightarrow T_3$ transition in 12-BAP needs to overcome a minimal energy barrier (5.5 meV) compared to the $S_1 \rightarrow T_4$ transition in 12-FAP and 12-CAP. The Br atom proximal to the pyridinic N in 12-BAP lowered the $^3n\pi^*$ state energy through sidewise orbital interactions (Fig. 2). Hence, the proximity between the Br atom and pyridinic N in 12-BAP not only enhanced the SOC ($89\ cm^{-1}$) but also tuned the $^3n\pi^*$ state energy to a favourable position, which enabled the $^1\pi\pi^* \rightarrow {}^3n\pi^*$ transition to occur on an ultrafast timescale.

The comparison of k_{isc} for the most effective ISC channels in AP and 12-XAP is shown in Fig. 3. Since the k_{isc} ($S_1 \rightarrow T_2$) in AP and 12-HAP is lower than their k_{fl}, ISC cannot quench their fluorescence. As a result, AP and 12-HAP exhibit intense fluorescence, as observed in previous experiments.[45,46] In contrast, halogen substitution at the 12-position of AP increased the ISC rate, primarily guided by the change in state character between S_1 and T_n states. The $S_1 \rightarrow T_4$ ISC channel in 12-FAP and 12-CAP originates from the $^1\pi\pi^* \rightarrow {}^3n\pi^*$ transition, leading to an increased ISC rate. The ISC rate of 12-FAP is more than twice as fast as its fluorescence rate, which may result in a reduced fluorescence quantum yield. Meanwhile, 12-CAP cannot fluoresce, as its ISC rate is three orders of magnitude faster than its fluorescence rate. The ISC rate for the $S_1 \rightarrow T_3$ channel in 12-BAP is the highest among all the channels and is four orders of magnitude faster than its fluorescence rate. Therefore, ISC effectively quenched the fluorescence in 12-BAP.

We strategically designed a structural motif where the bromine atom proximal to the pyridinic nitrogen in 12-BAP boosts ISC. This enhancement of ISC originates from the interplay of three key factors: (i) the orbital angular momentum change during the $^1\pi\pi^* \rightarrow {}^3n\pi^*$ transition; (ii) the heavy atom effect; and (iii) the favourable energy gap between $^1\pi\pi^*$ and $^3n\pi^*$ states. To rationalize the design principles behind efficient triplet population *via* ISC, we explored how the variation of Br positions in AP influences SOC and ISC. While these positional changes did not affect the fluorescence rate ($k_{fl} \approx 10^8\ s^{-1}$; Table S6), they significantly modified the energy spacing and SOC between the $^1\pi\pi^*$ and $^3n\pi^*$ states (Table S7). The $^3n\pi^*$ state of 2-BAP (T_7) was about 1.0 eV above the S_1 state at the S_1-geometry and had strong SOC ($\sim 35.86\ cm^{-1}$) with the S_1 ($^1\pi\pi^*$) state. Shifting the Br atom from the 2- to 3-position in AP lowered the $^3n\pi^*$ state energy (T_6) by 0.15 eV and reduced the SOC by $6\ cm^{-1}$. A further shift to 4-BAP slightly reduced the $^3n\pi^*$ state energy (T_6) by 0.06 eV, while SOC dropped more sharply by $21\ cm^{-1}$. The energy spacing between the $^1\pi\pi^*$ and $^3n\pi^*$ (T_6) states remained mostly unchanged, fluctuating slightly between 0.68 and 0.78 eV, as Br was placed at various sites ranging from 4 to 11. Meanwhile, the SOC between these states remained within the range of 4.2 to $8.7\ cm^{-1}$. Substituting Br at the 12-position of AP substantially altered the electronic structure, bringing the $^3n\pi^*$ state (now T_3 in 12-BAP) closer to the $^1\pi\pi^*$ (S_1) state (ΔST = 0.15 eV). Moreover, the SOC between these states ($89\ cm^{-1}$) reached the highest value among all observed cases.

Fig. 4 illustrates how the SOC, *i.e.*, $\langle {}^1\pi\pi^*|\hat{H}_{so}|{}^3n\pi^*\rangle$, varied with the distance between the Br atom and the pyridinic N. In 2-BAP, R is around 2.75 Å, the nearest distance between Br and N among all the systems. The SOC in 2-BAP is significantly strong ($36\ cm^{-1}$). However, when the Br atom shifts from 2 to 3, the R value increased to ~ 4 Å and the SOC reduced to $30\ cm^{-1}$. When R exceeded 5 Å, with Br positioned between 4 and 11, the SOC sharply decreased to a low value ranging from 4 to $8\ cm^{-1}$. In 12-BAP, the Br atom is closer to N, with R below 3 Å. Consequently, the SOC is the highest among all the systems, approaching $89\ cm^{-1}$. Since $\hat{H}_{so} \propto Z^4$ (Z is the nuclear charge), a heavy Br atom near the n-orbital of pyridinic-N (at the site of ΔL) can induce strong $\langle {}^1\pi\pi^*|\hat{H}_{so}|{}^3n\pi^*\rangle$ through the HAE. When

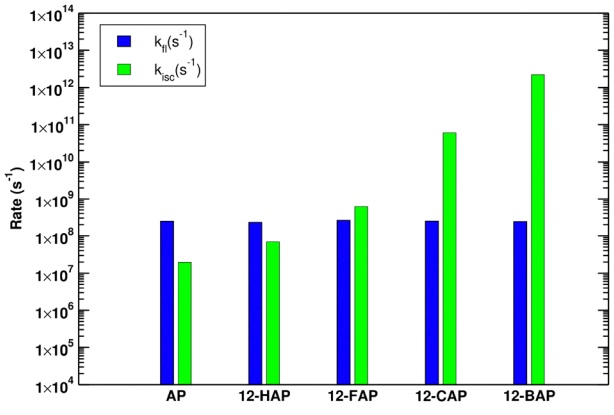

Fig. 3 Comparison of the fluorescence and ISC rate constants for AP and 12-XAP.

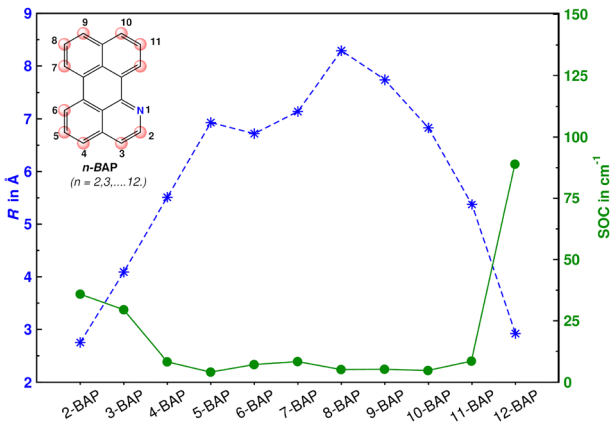

Fig. 4 Distance between Br and N (R in Å) in n-BAP and the SOC between the $^1\pi\pi^*$ and $^3n\pi^*$ states ($\langle {}^1\pi\pi^*|\hat{H}_{so}|{}^3n\pi^*\rangle$ in cm^{-1}).

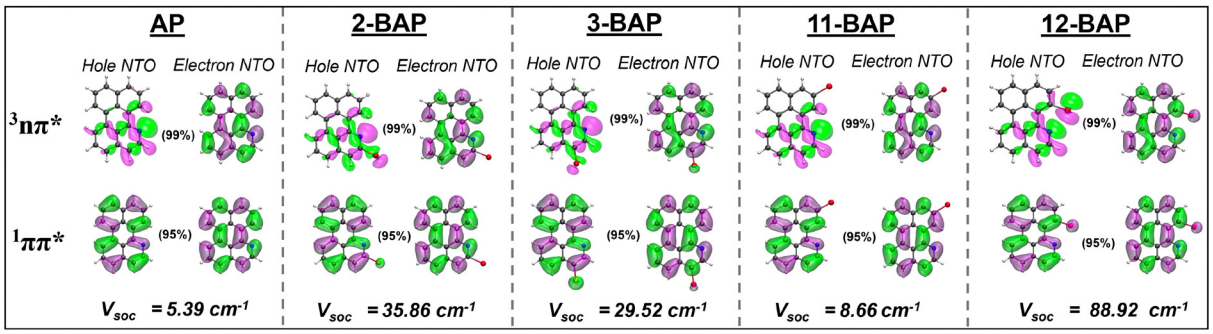

Fig. 5 Natural transition orbitals of the $^1\pi\pi^*$ and $^3n\pi^*$ states for AP, 2-BAP, 3-BAP, 11-BAP and 12-BAP.

comparing 2-BAP and 12-BAP, the R value of 2-BAP (2.75 Å) is lower than that of 12-BAP (2.95 Å), while the SOC is higher for 12-BAP. This contrasting behaviour can be rationalized using the NTO plot shown in Fig. 5. In AP, the n-orbital is localized on the pyridinic N, whereas in 2-BAP, the n-orbital extends in-plane with mutual alignment of the p-orbital of Br. This extension is weaker in 3-BAP and absent in 4-BAP to 11-BAP (see Fig. S3). In 12-BAP, the n-orbital exhibited greater spatial extension due to its side-wise association with the in-plane p-orbital of Br. Fig. 5 illustrates that this p-orbital of Br contributed prominently to the hole NTO of the $^3n\pi^*$ state, in conjunction with the n-orbital of N. This cooperative orbital mixing leads to an expanded hole NTO for the $^3n\pi^*$ state, which is orthogonal to the hole NTO of the $^1\pi\pi^*$ state. Consequently, the SOC matrix element ($\langle^1\pi\pi^*|\hat{H}_{so}|^3n\pi^*\rangle$) is significantly enhanced in 12-BAP.

Furthermore, we computed the ISC rates for the nearby $^3\pi\pi^*$ state and the $^3n\pi^*$ state of n-BAP, as summarized in Table S8. The $S_1 \rightarrow T_2$ ISC channel in n-BAP corresponds to the $^1\pi\pi^* \rightarrow {}^3\pi\pi^*$ transition. Despite the weak SOC, the ISC remained energetically favourable ($\Delta G < 0$), yielding k_{isc} in the 10^{5-7} s^{-1} range. For the alternative ISC channel ($^1\pi\pi^* \rightarrow {}^3n\pi^*$), k_{isc} was quite low ($\sim 10^3$ s^{-1}) for 2-BAP and varied between 10^{5-6} s^{-1} for the other derivatives, except for 12-BAP (where it reached 10^{12} s^{-1}). Although the SOC was higher for $^1\pi\pi^* \rightarrow {}^3n\pi^*$ than for $^1\pi\pi^* \rightarrow {}^3\pi\pi^*$, the ISC for $^1\pi\pi^* \rightarrow {}^3n\pi^*$ remained inefficient across 2-BAP to 11-BAP due to the unfavourable driving force ($\Delta G > 0$) and substantial barrier height (220–480 meV). While strong SOC allows spin-forbidden transitions, it alone does not ensure rapid ISC. In the Marcus framework (refer to eqn (3)), the ISC rate constant scales quadratically with SOC but decays exponentially with ΔG. An uphill singlet–triplet energy gap ($\Delta G > 0$) can therefore outweigh the benefit of large SOC, so both strong coupling and favourable energetic alignment are required for efficient triplet formation. In 12-BAP, the $^1\pi\pi^* \rightarrow {}^3n\pi^*$ transition was significantly more efficient, surpassing the $^1\pi\pi^* \rightarrow {}^3\pi\pi^*$ by four orders of magnitude, which was driven by remarkably high SOC ($\langle^1\pi\pi^*|\hat{H}_{so}|^3n\pi^*\rangle$ = 89 cm^{-1}), and an energetically favourable process ($\Delta G < 0$) with a low activation barrier (5.5 meV). Table 4 summarizes the k_{isc} values for the dominant ISC channel in AP and several bromo-substituted derivatives.

Table 4 Calculated ISC rate constants (k_{isc} in s^{-1}) for AP and several bromo-substituted derivatives with the spin–orbit coupling (V_{soc} in cm^{-1}), electronic energy difference (ΔG in meV), reorganization energy (E_r in meV), and activation energy (E_a in meV). SOC matrix elements were evaluated using the effective one-electron SO operator with Chiodo-derived Z_{eff} values

Molecule	$\lvert V_{soc}\rvert$	ΔG	E_r	E_a	k_{isc}
AP	0.20	−42.5	114.3	11.3	1.96×10^7
2-BAP	0.13	−10.3	109.0	22.3	5.55×10^6
3-BAP	0.23	−16.3	109.5	19.8	1.91×10^7
11-BAP	0.18	−32.5	116.2	15.1	1.37×10^7
12-BAP	88.92	−436.5	546.4	5.5	2.22×10^{12}

Notably, Br proximal to the pyridinic N facilitated an ultrafast triplet population *via* ISC in 12-BAP owing to the enhanced SOC and the optimized energy alignment between the $^1\pi\pi^*$ and $^3n\pi^*$ states.

Conclusions

In conclusion, we computationally designed a new structural motif, *i.e.*, 12-BAP, by functionalizing a bromine atom near the nitrogen at the bay site of AP to enhance ISC. The HAE from Br significantly strengthened SOC ($\langle^1\pi\pi^*|\hat{H}_{so}|^3n\pi^*\rangle$ = 89 cm^{-1}), enabling ultrafast ISC (10^{12} s^{-1}) that outcompetes fluorescence. In contrast, AP and 12-HAP remained fluorescent due to their higher $^3n\pi^*$ state energies. Br substitution at the 2-, 3-, and 12-positions increased the $\langle^1\pi\pi^*|\hat{H}_{so}|^3n\pi^*\rangle$ *via* HAE, with 12-BAP showing the strongest effect. Despite its shortest Br···N distance, 2-BAP exhibited lower SOC than 12-BAP because the stronger lateral interaction in 12-BAP leads to greater extension of the hole NTO. This lateral interaction in 12-BAP also lowered the $^3n\pi^*$ state energy, facilitating rapid ISC, while 2-BAP retained a higher, less favourable energy for the $^3n\pi^*$ state, which limited its ISC efficiency. Thus, the strategic design of 12-BAP integrates three key elements that collectively facilitate ultrafast ISC: (i) the orbital angular momentum change during singlet–triplet conversion ($^1\pi\pi^* \rightarrow {}^3n\pi^*$), (ii) a pronounced HAE, and (iii) a narrow energy gap between the $^1\pi\pi^*$ and $^3n\pi^*$ states. The development of efficient phosphorescent organic materials relies on promoting ISC from the S_1 to the triplet state. Moreover, in PDT, the photosensitizer transfers its triplet

energy to ground-state molecular oxygen ($^3O_2$), generating reactive singlet oxygen ($^1O_2$). Hence, ISC-mediated conversion of singlet to triplet excitons plays a crucial role in both organic optoelectronic performance and PDT efficacy. This work introduces a design principle for enhancing ISC, and we anticipate that the proposed spin-conversion strategy will significantly advance both metal-free OLEDs and PDT.

Author contributions

PD contributed to data curation, methodology, formal analysis, investigation, visualization, and manuscript writing and revision. SD was involved in data curation, methodology, formal analysis, and visualization. SS led the project's conceptualization and supervision, and contributed to methodology, investigation, formal analysis, and manuscript writing and revision.

Conflicts of interest

There are no conflicts to declare.

Data availability

The data supporting this article have been included as part of the supplementary information (SI). Supplementary information: Frontier molecular orbitals of AP and 12-XAP at S_0 geometry, energy level diagram for frontier molecular orbitals at S_1 geometry, natural transition orbitals of n-BAP at S_1 geometry (Fig. S1–S3); excitation energies of AP and 12-XAP at S_0 and S_1 geometries; ΔST, SOC and singlet–triplet mixing coefficient between S_1 and T_n states of AP and its derivatives; scaling factors (Z_{eff}) utilized in effective one-electron spin–orbit operator, comparison of ΔST and SOC for 12-BAP across density functionals, details of ISC rate constants for AP and its derivatives, fluorescence rate constant of n-BAP (Table S1–S8); Cartesian coordinates for the optimized S_0, S_1 and T_n geometries of AP and 12-XAP (Table S9–S23). See DOI: **https://doi.org/10.1039/d5cp03115j.**

Acknowledgements

PD and SD gratefully thank NIT Tiruchirappalli and the Ministry of Education (Government of India) for their research fellowships. SS acknowledges the funding from the DST-SERB project (CRG/2021/002893). We thank DST-FIST (SR/FST/CS-II/2018/64) for providing access to the HPC facility.

References

1 C. W. Tang and S. A. VanSlyke, *Appl. Phys. Lett.*, 1987, **51**, 913–915.
2 M. A. Baldo, D. F. O'Brien, Y. You, A. Shoustikov, S. Sibley, M. E. Thompson and S. R. Forrest, *Nature*, 1998, **395**, 151–154.
3 T. C. Pham, V. N. Nguyen, Y. Choi, S. Lee and J. Yoon, *Chem. Rev.*, 2021, **121**, 13454–13619.
4 S. K. Lower and M. A. El-Sayed, *Chem. Rev.*, 1966, **66**, 199–241.
5 J. Zhao, W. Wu, J. Sun and S. Guo, *Chem. Soc. Rev.*, 2013, **42**, 5323–5351.
6 M. Schulze, A. Steffen and F. Würthner, *Angew. Chem., Int. Ed.*, 2015, **54**, 1570–1573.
7 O. Bolton, K. Lee, H.-J. Kim, K. Y. Lin and J. Kim, *Nat. Chem.*, 2011, **3**, 205–210.
8 O. Bolton, D. Lee, J. Jung and J. Kim, *Chem. Mater.*, 2014, **26**, 6644–6649.
9 M. S. Kwon, D. Lee, S. Seo, J. Jung and J. Kim, *Angew. Chem., Int. Ed.*, 2014, **53**, 11177–11181.
10 D. Lee, O. Bolton, B. C. Kim, J. H. Youk, S. Takayama and J. Kim, *J. Am. Chem. Soc.*, 2013, **135**, 6325–6329.
11 M. S. Kwon, Y. Yu, C. Coburn, A. W. Phillips, K. Chung, A. Shanker, J. Jung, G. Kim, K. Pipe and S. R. Forrest, *Nat. Commun.*, 2015, **6**, 8947.
12 M. S. Kwon, J. H. Jordahl, A. W. Phillips, K. Chung, S. Lee, J. Gierschner, J. Lahannabcd and J. Kim, *Chem. Sci.*, 2016, **7**, 2359–2363.
13 S. Hirata, K. Totani, J. Zhang, T. Yamashita, H. Kaji, S. R. Marder, T. Watanabe and C. Adachi, *Adv. Funct. Mater.*, 2013, **23**, 3386–3397.
14 S. Xiong, Y. Xiong, D. Wang, Y. Pan, K. Chen, Z. Zhao, D. Wang and B. Z. Tang, *Adv. Mater.*, 2023, **35**, 2301874.
15 R. D. Pensack, Y. Song, T. M. McCormick, A. A. Jahnke, J. Hollinger, D. S. Seferos and G. D. Scholes, *J. Phys. Chem. B*, 2014, **118**, 2589–2597.
16 A. J. Tilley, R. D. Pensack, T. S. Lee, B. Djukic, G. D. Scholes and D. S. Seferos, *J. Phys. Chem. C*, 2014, **118**, 9996–10004.
17 G. He, B. D. Wiltshire, P. Choi, A. Savin, S. Sun, A. Mohammadpour, M. J. Ferguson, R. McDonald, S. Farsinezhad, A. Brown, K. Shankar and E. Rivard, *Chem. Commun.*, 2015, **51**, 5444–5447.
18 R. Acharya, S. Cekli, C. J. I. Zeman, R. M. Altamimi and K. S. Schanze, *J. Phys. Chem. Lett.*, 2016, **7**, 693–697.
19 W. Shao, H. Jiang, R. Ansari, P. M. Zimmerman and J. Kim, *Chem. Sci.*, 2022, **13**, 789–797.
20 W. Shao and J. Kim, *Acc. Chem. Res.*, 2022, **55**, 1573–1585.
21 E. Hamzehpoor, C. Ruchlin, Y. Tao, C.-H. Liu, H. M. Titi and D. F. Perepichka, *Nat. Chem.*, 2023, **15**, 83–90.
22 D. R. Kearns and W. A. Case, *J. Am. Chem. Soc.*, 1966, **88**, 5087–5097.
23 E. Lim and J. M. Yu, *J. Chem. Phys.*, 1966, **45**, 4742–4743.
24 K. Schmidt, S. Brovelli, V. Coropceanu, D. Beljonne, J. Cornil, C. Bazzini, T. Caronna, R. Tubino, F. Meinardi, Z. Shuai and J. L. Brédas, *J. Phys. Chem. A*, 2007, **111**, 10490–10499.
25 S. Sarkar, J. D. Protasiewicz and B. D. Dunietz, *J. Phys. Chem. Lett.*, 2018, **9**, 3567–3572.
26 S. Sarkar, H. P. Hendrickson, D. Lee, F. DeVine, J. Jung, E. Geva, J. Kim and B. D. Dunietz, *J. Phys. Chem. C*, 2017, **121**, 3771–3777.

27 E. Lucenti, A. Forni, C. Botta, L. Carlucci, C. Giannini, D. Marinotto, A. Pavanello, A. Previtali, S. Righetto and E. Cariati, *Angew. Chem., Int. Ed.*, 2017, **56**, 16302–16307.
28 Y. Lee, R. M. Malamakal, D. M. Chenoweth and J. M. Anna, *J. Phys. Chem. Lett.*, 2020, **11**, 877–884.
29 W. Shao, J. Hao, H. Jiang, P. M. Zimmerman and J. Kim, *Adv. Funct. Mater.*, 2022, **32**, 2201256.
30 Y. He, J. Wang, Q. Li, S. Qu, C. Zhou, C. Yin, H. Ma, H. Shi, Z. Meng and Z. An, *Adv. Opt. Mater.*, 2023, **11**, 2201641.
31 K. Chen, Y. Xiong, D. Wang, Y. Pan, Z. Zhao, D. Wang and B. Z. Tang, *Adv. Funct. Mater.*, 2024, **34**, 2312883.
32 Y. Tani, K. Miyata, E. Ou, Y. Oshima, M. Komura, M. Terasaki, S. Kimura, T. Ehara, K. Kubo, K. Onda and T. Ogawa, *Chem. Sci.*, 2024, **15**, 10784–10793.
33 C. Demangeat, M. Remond, T. Roisnel, C. Quinton and L. Favereau, *Chem. – Eur. J.*, 2024, **30**, e202401506.
34 K. Vinod, S. D. Jadhav and M. Hariharan, *Chem. – Eur. J.*, 2024, **30**, e202400499.
35 D. Shikichi, T. Ehara, M. Komura, K. Onda, K. Miyata and Y. Tani, *J. Chem. Phys.*, 2025, **162**, 121101.
36 S. M. Wagalgave, A. A. Kongasseri, U. Singh, A. Anilkumar, S. N. Ansari, S. K. Pati and S. J. George, *J. Am. Chem. Soc.*, 2025, **147**, 15591–15601.
37 J. T. Markiewicz and F. Wudl, *ACS Appl. Mater. Interfaces*, 2015, **7**, 28063–28085.
38 A. A. Rachford, S. Goeb and F. N. Castellano, *J. Am. Chem. Soc.*, 2008, **130**, 2766–2767.
39 Y.-L. Lee, Y.-T. Chou, B.-K. Su, C.-C. Wu, C.-H. Wang, K.-H. Chang, J.-A. A. Ho and P.-T. Chou, *J. Am. Chem. Soc.*, 2022, **144**, 17249–17260.
40 Y. Wu, Y. Zhen, Y. Ma, R. Zheng, Z. Wang and H. Fu, *J. Phys. Chem. Lett.*, 2010, **1**, 2499–2502.
41 J. Sunny, E. Sebastian, S. Sujilkumar, F. Würthner, B. Engels and M. Hariharan, *Phys. Chem. Chem. Phys.*, 2023, **25**, 28428–28436.
42 P. Durairaj, D. Mukkonathil and S. Sarkar, *J. Phys. Chem. A*, 2024, **128**, 10193–10201.
43 Y. Wu, X. Liu, J. Liu, G. Yang, Y. Deng, Z. Bin and J. You, *J. Am. Chem. Soc.*, 2024, **146**, 15977–15985.
44 D. T. Gryko, J. Piechowska and M. Gałęzowski, *J. Org. Chem.*, 2010, **75**, 1297–1300.
45 I. Deperasińska, D. T. Gryko, E. Karpiuk, B. Kozankiewicz, A. Makarewicz and J. Piechowska, *J. Phys. Chem. A*, 2012, **116**, 2109–2116.
46 A. Hirono, H. Sakai, S. Kochi, T. Sato and T. Hasobe, *J. Phys. Chem. B*, 2020, **124**, 9921–9930.
47 P. Hohenberg and W. Kohn, *Phys. Rev.*, 1964, **136**, B864–B871.
48 W. Kohn and L. J. Sham, *Phys. Rev.*, 1965, **140**, A1133–A1138.
49 M. E. Casida, C. Jamorski, K. C. Casida and D. R. Salahub, *J. Chem. Phys.*, 1998, **108**, 4439–4449.
50 S. Hirata and M. Head-Gordon, *Chem. Phys. Lett.*, 1999, **314**, 291–299.
51 J. S. Sears, T. Koerzdoerfer, C.-R. Zhang and J.-L. Brédas, *J. Chem. Phys.*, 2011, **135**, 151103.
52 M. J. G. Peach, M. J. Williamson and D. J. Tozer, *J. Chem. Theory Comput.*, 2011, **7**, 3578–3585.
53 J.-D. Chai and M. Head-Gordon, *Phys. Chem. Chem. Phys.*, 2008, **10**, 6615–6620.
54 J.-D. Chai and M. Head-Gordon, *J. Chem. Phys.*, 2008, **128**, 084106.
55 M. M. Francl, W. J. Pietro, W. J. Hehre, J. S. Binkley, M. S. Gordon, D. J. DeFrees and J. A. Pople, *J. Chem. Phys.*, 1982, **77**, 3654–3665.
56 K. D. Closser, O. Gessner and M. Head-Gordon, *J. Chem. Phys.*, 2014, **140**, 134306.
57 E. Epifanovsky, A. T. B. Gilbert, X. Feng, J. Lee, Y. Mao, N. Mardirossian, P. Pokhilko, A. F. White, M. P. Coons and A. L. Dempwolff, *et al.*, *J. Chem. Phys.*, 2021, **155**, 084801.
58 S. J. Strickler and R. A. Berg, *J. Chem. Phys.*, 1962, **37**, 814–822.
59 R. A. Marcus, *Rev. Mod. Phys.*, 1993, **65**, 599–610.
60 Q. Ou and J. E. Subotnik, *J. Phys. Chem. C*, 2013, **117**, 19839–19849.
61 D. G. Fedorov and M. S. Gordon, *J. Chem. Phys.*, 2000, **112**, 5611–5623.
62 S. Kotaru, P. Pokhilko and A. I. Krylov, *J. Chem. Phys.*, 2022, **157**, 224110.
63 J. Ehrman, E. Martinez-Baez, A. J. Jenkins and X. Li, *J. Chem. Theory Comput.*, 2023, **19**, 5785–5790.
64 J. J. Talbot, T. P. Cheshire, S. J. Cotton, F. A. Houle and M. Head-Gordon, *J. Phys. Chem. A*, 2024, **128**, 7830–7842.
65 A. Van Yperen-De Deyne, E. Pauwels, V. Van Speybroeck and M. Waroquier, *Phys. Chem. Chem. Phys.*, 2012, **14**, 10690–10704.
66 S. Koseki, M. S. Gordon, M. W. Schmidt and N. Matsunaga, *J. Phys. Chem.*, 1995, **99**, 12764–12772.
67 S. Koseki, M. W. Schmidt and M. S. Gordon, *J. Phys. Chem.*, 1992, **96**, 10768–10772.
68 S. Koseki, M. W. Schmidt and M. S. Gordon, *J. Phys. Chem. A*, 1998, **102**, 10430–10435.
69 S. G. Chiodo and N. Russo, *J. Comput. Chem.*, 2008, **30**, 832–839.
70 F. Lewitzka, H.-G. Lühmannsrijben, M. Strauch and W. Lüttke, *J. Photochem. Photobiol. A*, 1991, **61**, 191–200.
71 F. Weigend and R. Ahlrichs, *Phys. Chem. Chem. Phys.*, 2005, **7**, 3297–3305.
72 J. Dunning and H. Thom, *J. Chem. Phys.*, 1989, **90**, 1007–1023.
73 M. K. Lee, P. Hoerner, W. Li and H. B. Schlegel, *J. Chem. Phys.*, 2020, **153**, 244109.
74 J. Liu, Z. Lan and J. Yang, *Phys. Chem. Chem. Phys.*, 2021, **23**, 22313–22323.
75 P. Durairaj, K. Samuthirapandi and S. Sarkar, *J. Phys. Chem. A*, 2023, **127**, 3330–3338.